Insights into copper electrochemical migration through numerical modeling and Monte Carlo simulation

Ali Dayoub, Ali Gharaibeh [*], Balázs Illés, Bálint Medgyes

Budapest University of Technology and Economics, Faculty of Electrical Engineering and Informatics, Department of Electronics Technology, Budapest, Hungary

ARTICLE INFO

ABSTRACT

Electrochemical migration (ECM) is receiving increased attention and requires further investigations due to the continuous miniaturization in microelectronics. A numerical ECM model for copper was developed which describes the anodic dissolution using two approaches: a constant anodic surface concentration and an increasing anodic dissolution rate, modeling the ion transport using the Nernst–Planck equation, simulates the dendrite growth was stochastically using the Monte Carlo method. The results of the numerical model were validated by water-drop (WD) tests using pure copper electrodes in a contaminant-free electrolyte. The validation process involved comparing the time to failure (TTF) values and the morphology of the dendrites. The incubation analysis of the numerical model reveals that diffusion dominates the early stages of the process, but eventually transitions into a diffusion-migration-controlled mechanism, with migration being higher near the anode and diffusion remaining dominant closer to the cathode. The Monte Carlo simulation demonstrated both efficiency and flexibility in modeling dendrite growth. The model also demonstrated that dendrite growth can be expressed as a function of copper ion concentration and the strength of the electric field across the gap between the cathode and anode. Our model could be a useful tool for ECM failure prediction and further ECM research as the digital twin of the ECM process.

1. Introduction

The ongoing trend of miniaturization and high-density design in the microelectronics industry has brought increased attention to certain reliability issues. One of the most significant of these is electrochemical migration (ECM), which is a humidity-induced failure on printed circuit boards (PCBs) [1,2]. ECM typically arises between adjacent electrodes with opposite biases when they are connected by an electrolyte layer. This leads to the dissolution of metal at the anode, and the resulting cations transport through the electrolyte to the cathode, where they electrochemically reduce. As reduction continues at the cathode, metallic dendrites form and extend toward the anode. The dendrite growth can eventually cause a short circuit, leading to malfunction or failure of the microelectronic device. The modeling of the ECM process can be divided into two key stages: dendrite incubation and growth [3, 4]. The incubation stage includes the formation of the electrolyte layer, the dissolution of the anode, and the movement of cations, which prepares for dendrite development. The growth stage begins with the initiation of dendrites and continues until an electrical short circuit

occurs. The combined duration of these stages represents the time to failure (TTF) of the sample [5,6].

Understanding the ECM process is critical since many of the metals used in microelectronics assembly—such as Sn [7], Pb [8], Ag [9], Cu [10], and Zn [11]—are susceptible to ECM in various ways. Extensive experimental research has been conducted to explain their susceptibility under different conditions, including their presence as pure metals or alloys, varying voltage levels, contamination levels, and different testing methods [12,13]. A notable recent finding in ECM research is the discovery that Au can undergo ECM in a contaminant-free electrolyte [14, 15], previously it was considered to be resistant. This emphasizes the need for further research to understand and analyze the susceptibility of the various metals used in microelectronics.

In recent years, significant progress has been made in ECM process modeling research. For instance, Yang et al. [16] created a comprehensive regression model for the ECM of Ag, based on failure physics and incorporating various temperature–humidity–bias stress conditions. Similarly, Zhou et al. [17] developed a lifetime model to analyze the effects of soluble salts at various concentrations on ECM failure in

immersion silver (ImAg)-plated PCBs. While these models represent important steps toward predicting the TTF of samples, machine learning-based models have proven to outperform them from the perspective of predictive accuracy [18–20]. However, while failure physics and machine learning models are valuable tools for predicting TTF, they do not fully explain the underlying physical processes involved in ECM or reliably predict TTF for ECM in electronic systems.

Numerical modeling is a valuable tool for gaining a deeper understanding of the ECM process. However, it is important to recognize that most existing numerical models have been developed to study electrochemical deposition (ECD) in electrochemistry rather than ECM on electronic systems [3,21–26]. He et al. [27,28] presented three main distinctions: (i) ECM involves a significantly thinner transport medium (electrolyte), (ii) lower ionic strength characterizes the transport medium, and (iii) electroactive or metal ions are not present before applying a potential difference. Thus, applying the theories of ECD in electrochemistry to ECM might have limitations. Despite this, He et al. [27] successfully compared these ECD models with their own 1D ECM model for Cu utilizing the Nernst–Planck equation and impedance measurements. They concluded that their model is suitable for simulating ECM of copper in deionized (DI) water on PCBs by predicting the TTF of the sample, particularly in scenarios where no electroactive ions or supporting electrolytes are present before the application of a potential difference. This underscores the significant differences between ECD in electrochemistry and ECM on electronics, which limit the applicability of ECD models for studying ECM. Furthermore, the morphology of the dendrites was not examined in their work.

To address this, Illés et al. [29] developed a 2D numerical model of the entire ECM process for Cu, where the anodic dissolution and ion transport steps were modeled deterministically using the Nernst–Planck equation, while dendrite growth was modeled stochastically using a specially developed algorithm. This model not only provided accurate predictions of TTF and validated them against experimental data but also effectively simulated the dendrite morphology, showing a tree-like structure. Cao et al. [30] further confirmed predictions of dendrite morphology by employing the phase-field method to study the ECM of silver-based conductive adhesives. Ma et al. [31] successfully investigated the incubation period of ECM in the Sn-9 Zn solder alloy in DI water-electrolyte by visualizing the concentration profiles of Sn^{2+} and Zn^{2+} ions as a function of the distance between the anode and cathode, using numerical solutions of the Nernst–Planck transport equation. The results revealed that the advection rate of the highly soluble and diffusible Zn^{2+} ions is greater than that of Sn^{2+} ions, which may explain the higher proportion of zinc in the dendrites formed in some cases, despite the significantly higher tin content in the Sn-9 Zn solder alloy. Xue et al. [32] conducted a case study on predicting ECM-induced failure in a gate driver circuit board by using surface insulation resistance (SIR) measurements to calibrate the exchange current densities of the electrochemical reaction. By employing leakage current as an indicator of the initial onset of ECM, they predicted ECM-induced failure based on the simulated current density.Ható et al. [33] utilized the Brownian dynamics simulation technique to model the electrodiffusion of Sn ions and dendrite growth, demonstrating good agreement with the experimental water drop (WD) test results.

The previous studies [27–33] have offered valuable insights into the mechanism of the ECM process. However, a detailed analysis of ion transport remains lacking, particularly in examining the concentration behavior along the gap distance and the respective contributions of diffusion and migration to the overall transport process. Moreover, methods for effectively modeling dendrite growth are still scarcely addressed in the existing literature. Therefore, this work aims to deliver a comprehensive analysis of the entire ECM process of Cu through numerical modeling, focusing on the ion transport step mechanism and utilizing Monte Carlo simulation to model dendrite growth.

2. Numerical model of the ECM

2.1. Deterministic part of the ECM model

The step of electrolyte layer formation was not investigated, it was supposed that a droplet of DI water already bridged the electrodes. The ECM process begins with the dissolution of Cu at the anode, during which Cu^{2+} ions are directly formed at the anode [34,35], as expressed in Eq. (1). If the bias voltage is sufficiently high, oxygen evolution from water dissociation also occur at the anode surface, as expressed in Eq. (2) [13]:

$$Cu \rightarrow Cu^{2+} + 2e^- \tag{1}$$

$$2H_2O \rightarrow O_2 + 4H^+ + 4e^- \tag{2}$$

At the cathode, the primary reactions involve the reduction of the transported Cu^{2+} ions, which drives the growth of Cu metallic dendrites, and the reduction of water, as described in Eqs. (3) and (4) [34,35], respectively.

$$Cu^{2+} + 2e^- \rightarrow Cu \tag{3}$$

$$2H_2O + 2e^- \rightarrow H_2 + 2OH^- \tag{4}$$

The dissolution of Cu increases the ionic conductivity in the electrolyte droplet gradually. The conductivity increase is primarily influenced by the concentration of dissolved Cu^{2+} ions, which have a significantly greater impact on the conductivity compared to the formation of hydrogen [36]. Therefore, the amount of Cu dissolved at the anode can be modeled as in (5) [17]:

$$\Delta C_{an} = \frac{\varphi_{an} \times M \times (\sigma_0 + c \times q \times \mu)}{F \times n \times V_{drop}} \Delta t \tag{5}$$

where φ_{an} is the applied potential at the anode, M is the molar mass of Cu^{2+} ions, σ_0 is the electrical conductivity of DI water, c is the concentration of Cu^{2+} ions, q is the charge of Cu^{2+} ions ($n \times e$ where n is the chemical valence of Cu^{2+} ions and e is the elementary charge), μ is the mobility of Cu^{2+} ion, Δt is the time step of the simulation, F is the Faraday constant, and V_{drop} is the volume of the DI droplet. Besides the anodic dissolution mechanism proposed in Eq. (5), the concentration of Cu^{2+} ions at the anode may also be represented by a constant anodic surface concentration, denoted as c_{max}. This value reflects the "theoretical" maximum concentration of Cu^{2+} ions at the anode at 293 K [37]. In the interior region where ion transport occurs, the potential distribution can be determined using Poisson's equation for electrostatics. However, considering the criterion of electroneutrality in the electrolyte, it follows that the net charge density, ρ, is effectively zero simplifying Poisson's equation to Laplace's equation. Therefore, the potential distribution and the electric field between the electrodes can be computed as Eqs. (6) and (7), respectively.

$$\nabla^2 \varphi = \frac{\partial^2 \varphi}{\partial x^2} + \frac{\partial^2 \varphi}{\partial y^2} = 0 \tag{6}$$

$$\overline{E} = -\nabla\varphi = -\left(\frac{\partial \varphi}{\partial x}; \frac{\partial \varphi}{\partial y}\right) \tag{7}$$

Furthermore, in the context of ion transport, the contribution of electroconvection to the overall transport in ECM on PCBs is minimal. As a result, Cu^{2+} ions formed at the anode primarily transport through the electrolyte toward the cathode, following the electric field lines. The ion transport process is governed by the Nernst–Planck equation as in Eq. (8), which accounts for both diffusion and migration. Diffusion moves ions from areas of high concentration to low concentration, while migration drives ions in the direction of the electric field:

$$\overline{J} = -D\nabla c - \mu c \nabla \varphi \tag{8}$$

where J is the mass flux of Cu^{2+} ions, D is the diffusion coefficient of Cu^{2+} ion, c is the concentration of Cu^{2+} ions. In the absence of homogeneous reactions, the transient concentration changes of Cu^{2+} ions within the electrolyte droplet can be described by the continuity Eq. (9), which further enables the computation of Cu^{2+} ion concentrations within the grid as in Eq. (10):

$$\frac{\partial c}{\partial t} = -\nabla . J \tag{9}$$

$$\frac{\partial c}{\partial t} = D\nabla^2 c + \mu \nabla c . \nabla \varphi \tag{10}$$

2.2. Stochastic part of the ECM model

The stochastic part of the ECM model is the growth of dendrites, which begins at the cathode and later continues at the tips of the dendrites, where transported Cu^{2+} ions are reduced. Therefore, dendrites can be thought of as moving cathodes, necessitating updates to the electric potential and electric field (Eqs. (6) and (7)) after each reduction step.

The mechanism of dendrite growth in this simulation is based on a Monte Carlo simulation [38,39]. The simulation begins with dendrite initiation at the cathode and attempts to extend the dendrites by selecting random neighboring grid points across the grid, simulating the stochastic nature of dendrite formation. This random movement, or random walk, continues until the simulated particle encounters an existing dendritic structure. Dendrites can only grow when they come into contact with existing structures or originate from the cathode, making this step critical in the simulation process. Once a random site is identified as being in contact with an existing dendrite, it becomes a candidate for growth. The Monte Carlo simulation then evaluates the growth probability at this site, which is influenced by two key factors: the local electric field strength and the local Cu^{2+} ions concentration. In regions with higher Cu^{2+} ion concentrations [29] and stronger electric fields [7], the probability of reduction increases. These factors are normalized and combined into a weighted formula to calculate the growth probability, as shown in Eq. (11). The concentration is normalized by dividing its value by c_{max}. Meanwhile, E_{max} represents the maximum magnitude of the electric field within the grid, calculated at each Δt of the simulation. This approach reflects the Monte Carlo principle of evaluating potential outcomes based on probabilistic influences.

$$\text{growth\_probability} = k_1 \times \frac{c}{c_{max}} + k_2 \times \frac{E}{E_{max}} \tag{11}$$

where k_1 and k_2 are constants of normalized concentration and normalized electric field, respectively (the precise values are provided in the Results section). A random number between 0 and 1 is generated to determine if growth occurs. If this random number is less than the calculated growth probability, dendritic growth takes place at the site. In the case of growth, the local concentration of Cu^{2+} ions is set to zero because the ions were used up to form the dendrite. The electric field at that point is also set to zero to mimic the metallic nature of the dendrites, which no longer support ion migration. This probabilistic decision-making process is a hallmark of the Monte Carlo simulation, where multiple random events and outcomes are evaluated to model real-world phenomena. In each step, the Monte Carlo method performs multiple growth attempts (N) at different randomly selected sites. Each attempt is independent, with its probability of success based on the local conditions at that specific location (concentration and electric field). This probabilistic approach effectively mimics the real growth of dendrites, where growth occurs at specific sites due to localized factors rather than uniformly across the entire surface. The simulation continues through these iterations until one eventually touches the anode, signifying a system failure.

The numerical conversion and discretization of the partial differential equations (Eqs. (6), (7), and (10)) were performed using the Finite Difference Method (FDM). The computational ECM model was scripted and implemented using Python programming language. The 2D grid was constructed by meshing a set number of points in the x-direction (nx) and the y-direction (ny). The spacing between each point in the x-direction is (Δx), while the spacing between each point in the y-direction is (Δy). In each step, the Cu^{2+} concentration at the anode is increased according to Eq. (5), ensuring it does not exceed c_{max}. Meanwhile, the Cu^{2+} concentration at the cathode is set to match the concentration of the neighboring cells from the previous step, maintaining zero mass outflux of Cu^{2+} ions at that location. Table 1 lists the parameters used, while Table 2 outlines the initial and boundary conditions. Fig. 1 illustrates the entire ECM simulation process through a pseudocode representation.

2.3. Validation of the computational ECM model

The applicability of the computational ECM model was validated through experimental WD tests. In the WD test, a precisely defined volume and concentration of a droplet is artificially introduced between the electrodes to simulate the formation of the electrolyte layer. The droplet must adequately cover the electrodes and the space between them to provide a pathway for ion transport. Typically, the droplet volume ranges from 10 to 20 μl. In the current study, 15 μl of DI water is placed between the electrodes to represent a contaminant-free electrolyte. Ten WD tests were conducted for each case to obtain enough TTF and morphological data for validation of the ECM model.

3. Results and discussions

3.1. Model validation

Fig. 2a presents boxplots summarizing the variability in TTF results for both experimental and simulation data. It should be noted that the computed TTF data is generated by allowing N to take a random value between 1 and 70 in each step of the calculations, resulting in 2857 to 200,000 dendrite growth attempts per second. This wide range of dendrite growth attempts likely reflects the inherent randomness of dendrite growth in the ECM process. For the experimental data, the observed values range from a minimum of 6.5 s to a maximum of 14.3 s. The first quartile (Q1), median (Q2), and third quartile (Q3) are 7.5 s, 9.5 s, and 12.8 s, respectively. This distribution demonstrates a relatively widespread in the experimental results, with a skew toward longer

Table 1
List of physical and grid configuration parameters used in the computational ECM model.

Parameter [Unit]	Symbol	Value
Molar Mass of Cu^{2+} Ion [g/mol]	M	63.54
Faraday constant [C/mol]	F	96,485.33
Electrical Conductivity of DI Water [S/m]	σ_0	0.055×10^{-6}
Chemical Valence of Cu^{2+} Ion	n	2
Elementary Charge [C]	e	1.6×10^{-19}
Mobility of Cu^{2+} Ion [m²/Vs]	μ*	5.56×10^{-8}
Theoretical Maximum Anodic Concentration of Cu^{2+} Ion [g/l]	c_{max}*	7.56×10^{-5}
Ambient Temperature [K]	T	293
Diffusion Coefficient of Cu^{2+} Ion [m²/s]	D	3.67×10^{-10}
Volume of the DI Drolet [μl]	V_{drop}	15
Number of Grid Points in the x-direction	nx	200
Number of Grid Points in the y-direction	ny	200
Spacing Between Each Grid Point in the x-direction [μm]	Δx	1
Spacing Between Each Grid Point in the y-direction [μm]	Δy	1
Gap Distance [μm]	d	200
Time Step [μs]	Δt	350

* The values of μ and c_{max} are obtained from reference [37].

Table 2

List of initial conditions and boundary conditions utilized in the computational ECM model.

Condition type	Location	ϕ [VDC]	Cu^{2+} ion concentration [g/l]
Initial Condition	Anode	10	0
	Cathode	0	0
Boundary Condition	Anode	10	$C_{an}^{k-1} + \Delta C_{an}$ *
	Cathode	0	C_{cath-1}^{k-1}

* k represents the simulation step, while ΔC_{an} is calculated at each step of the simulation using Eq. (5).

failure times, as highlighted by the interquartile range (IQR) of 5.3 s. In comparison, the simulation data show a narrower range of TTF values, with a minimum value of 7.28 s, Q1 at 9.95 s, Q2 at 10.6 s, Q3 at 11.85 s, and a maximum value of 13.4 s. The IQR for the simulation data is 1.9 s, which is significantly smaller than that of the experimental data, suggesting that the simulations exhibit less variability, despite the fact that the computed TTF data is generated by allowing the number of dendrite growth attempts (N) to take a random value between 1 and 70 at each calculation step, resulting in 2857 to 200,000 dendrite growth attempts per second, to reflect the inherent randomness of the dendrite growth process. The simulated median TTF (10.6 s) is slightly higher than the experimental median (9.5 s), which may reflect differences in the underlying assumptions of the simulation model compared to real-world conditions.

The narrower range and smaller IQR of the simulation results indicate that the Monte Carlo method, while capturing stochastic variability, produces a more consistent set of outcomes compared to the experimental data. This consistency is likely due to the controlled conditions and parameters in the simulation, as opposed to the broader range of uncertainties in experimental conditions, several factors. First, the droplet is placed manually between the electrodes, introducing variability in its position. Second, while a micropipette is used to place the droplet, its accuracy can vary slightly, affecting the droplet's volume and shape. Third, the actual distance between the electrodes may deviate from the ideal due to manufacturing defects, further influencing the contact area. These combined factors impact the interaction between the electrodes and the DI water droplet, leading to differences in current density and, consequently, variability in ECM behavior observed in the experimental WD tests [12].

The TTF datasets for both experimental and simulation results were analyzed using a 2-parameter Weibull distribution, characterized by the shape parameter (β) and scale parameter (η) [5,40]. The shape parameter indicates the failure rate trend over time, with $\beta > 1$ signifying an increasing failure rate, while the scale parameter represents the TTF value at the 63.2 percentile. For the experimental data, $\beta = 3.53$ and $\eta = 11.12$ s, whereas for the simulation data, $\beta = 6.82$ and $\eta = 11.22$ s. To assess the significance of the difference between the experimental and computed TTF datasets, contour plots were created (see Fig. 2b). If there were no overlap in the contours, it would indicate a significant

---

Pseudocode for Simulating ECM process:

```
1: Input Simulation parameters:
2:     Physical, grid configuration, simulation time, time step, etc.
3: Initialize Variables
4:     φ, c, Eₓ, E_y, dendrites.
5: Set Initial Conditions for φ and c at the boundaries.
6:     φ[:, 0] = 10, φ[:, -1] = 0
7:     c[:, 0] = 0, c[:, -1] = 0
8: Defining object-oriented Functions
9: ECM Simulation Loop
10:        For each interior grid point [i, j]:
11:            update φ (eq. 6).
12:            update Eₓ and E_y (eq. 7).
13:        Anodic Dissolution Step:
14:            calculate dissolution amount (eq. 5).
15:            c[:, 0] += dissolution amount s.t. c[:, 0] ≤ cₘₐₓ
16:        Ion Transport Step (Nernst-Planck):
17:        For each interior grid point [i, j]:
18:            calculate diffusion and migration terms.
19:            update c[i, j] (eq. 10)..
20:            c[:, -1] = c_prev[:, -2]
21:        Dendrite Initiation:
22:        If ∃ c[:, -1] > 0 then
23:            dendrites[:, -1] = True
24:                Monte Carlo Loop:
25:                    For each growth attempt at randomly point selected (x, y):
26:                        While (x, y) ∈ c[:, -1] and/or adjacent to existing dendrite
27:                            Calculate growth probability (eq. 11).
28:                            If random.random() < growth_probability then
29:                                dendrites[x, y] = True, c[x, y] = 0.
30:                Failure Condition:
31:                If ∃dendrites[:, 0] = True then
32:                    Return TTF
33:                    break.
34: END
```

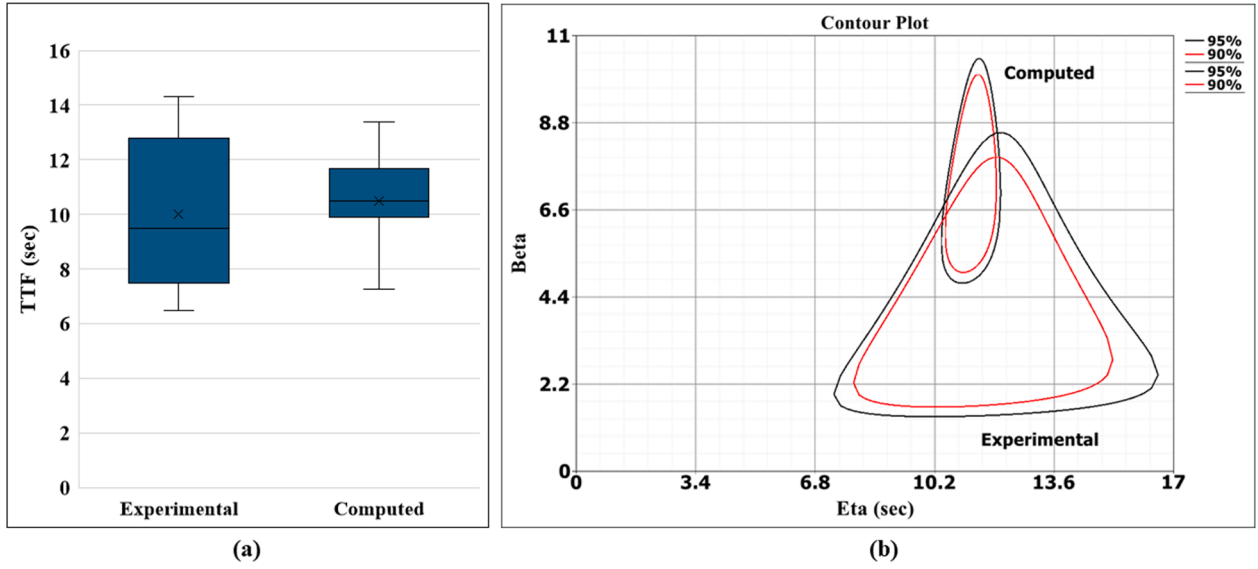**Fig. 1.** Pseudocode illustrating the ECM process of Cu.

Fig. 2. TTF validation process: (a) Comparison of experimental and computed TTF values, and (b) Contour plot illustrating the confidence levels of the experimental and computed TTF datasets.

difference [41,42]. However, no significant statistical difference was found, as the contours of both datasets overlapped at the 95 % and 90 % confidence levels.

3.2. Analysis of the incubation period

To have better understanding of the incubation period in ECM process, an analysis of the anodic dissolution and ion transport processes is necessary, as these phenomena play a key role in governing dendrite formation and growth at the cathode. Fig. 3 illustrates the concentration profiles of Cu ions, plotted as a function of the gap distance. In Fig. 3a, the concentration profile corresponds to an increasing anodic dissolution rate outlined in Eq. (5), while Fig. 3b shows the concentration profile, assuming a constant surface concentration at the anode, set equal to c_{max}, for comparison with the anodic dissolution mechanism outlined in Eq. (5). It can be observed that the concentration distribution follows an exponential pattern along the gap distance, regardless of the anodic dissolution mechanism used [27,29]. Furthermore, Fig. 3a indicates that the surface concentration is reached rapidly, even when the initial concentration at the anode is zero. This observation is consistent

with the findings of our former work [29], although the approach to the anodic dissolution step differed.

The contributions of diffusion and migration along the gap distance were analyzed during the incubation period by solving the first and second terms (representing diffusion and migration, respectively) on the right-hand side of Eq. (10) to gain deeper insight into the ion transport mechanism. Fig. 4 shows that the primary ion transport processes, migration and diffusion, follow an exponential pattern along the gap distance, which explains the exponential distribution of Cu ion concentrations along this distance in Fig. 3. In the early stages of incubation, diffusion is the dominant factor, being higher by 11 orders of magnitude at 0.5 s, 5 orders of magnitude at 1 s, 2 orders of magnitude at 2 s, and 1 order of magnitude at 3 s, as illustrated in Fig. 4a–d, respectively. However, after 4 s (Figs. 4e and F), the contributions of diffusion and migration become comparable, and migration starts to dominate near the anode. For instance, at 5 s (Fig. 4f), the ratio of the migration contribution to the diffusion contribution begins at 1.4 near the anode. As the distance from the anode increases along the gap, this ratio gradually decreases. At a point 18 μm away from the anode, the migration and diffusion contributions become equal. Beyond this point,
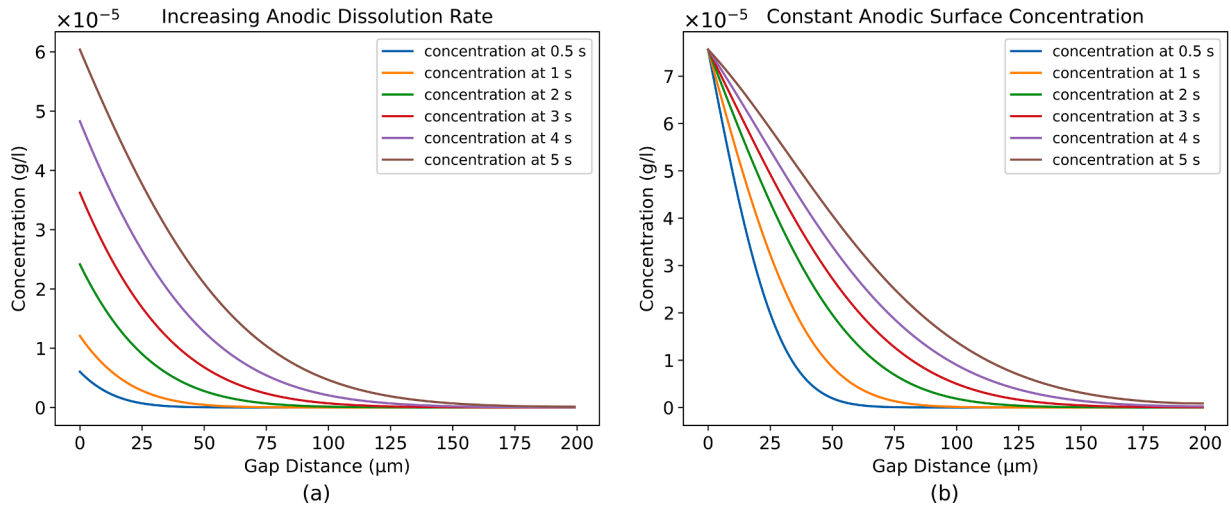

Fig. 3. Concentration profiles of Cu ions as a function of the gap distance (with 0 μm representing the anode and 200 μm the cathode) for (a) an increasing dissolution rate and (b) a constant surface concentration at the anode.
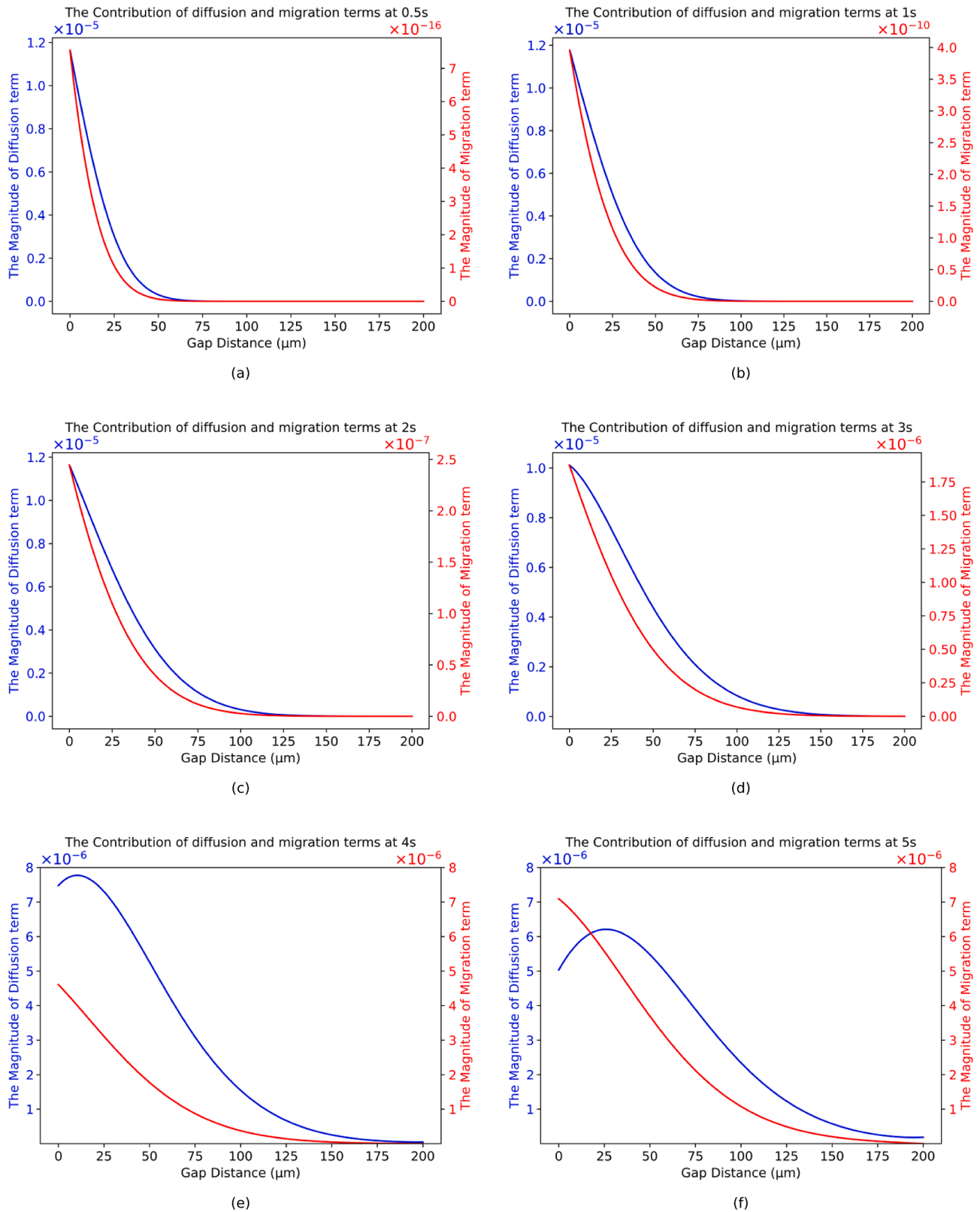
Fig. 4. Contributions of diffusion and migration terms as a function of the gap distance (with 0 μm representing the anode and 200 μm the cathode) during the incubation period of the process at: (a) 0.5 s, (b) 1 s, (c) 2 s, (d) 3 s, (e) 4 s, and (f) 5 s.

the ratio continues to decrease, dropping below 1 and eventually reaching a final value of 0.016 near the cathode which suggests that the ECM process is governed by both diffusion and migration mechanisms and their contribution percentage varies depending on position and

time. This observation goes beyond our previous findings, that the diffusion term consistently dominates, with an approximate ratio of 80/20 [29]. Furthermore, it is important to note that while eliminating the migration term would simplify the diffusion equation [43,44], it would

do so at the expense of accurately predicting the behavior of the ECM process, which restricts the applicability of some historical ECD models in electrochemistry, which only consider diffusion in the ion transport process.

3.3. Analysis of dendrite growth

Fig. 5 illustrates examples for the evolution of dendrites over the simulation time. The morphology of the computed Cu dendrites exhibits a ``tree-like'' structure. It was consistent with the optical images of the experimental Cu dendrites shown in Fig. 6. Furthermore, the "tree-like" structure of the numerical dendrites aligns with the morphologies of Cu dendrites reported in previous studies [35,45–47].

It was observed that dendrites initially form across the entire cathode region; however, over time, only a few dominant branches continue to grow within a given area, ultimately resulting in concentrated dendrites.

It was identical to the experimental results (Fig. 6.) and with our previous model, where the dendrite growth was modeled by a self-developed stochastic algorithm [29]. It should be noted that the specific location at the cathode where dendrites initiate remains random, influenced by factors such as surface morphology on the cathode surface, which facilitates preferred nucleation sites to start the initiation of the dendrites, which in turn, affect the overall range of dendrite growth across the cathode surface [48]. Additionally, other factors, such as the applied voltage level, also influence the growth process, further contributing to the variability in dendrite formation. At higher voltages, for instance, the strong electric field enables the dissolved metal ions from the anode to rapidly reach the cathode, limiting their ability to diffuse and find the lowest energy deposition point, resulting in random deposition. Additionally, at large voltages, the intensified hydrogen evolution reaction at the cathode can promote random deposition due to bubble agitation, leading to widespread metal nucleation and a broad
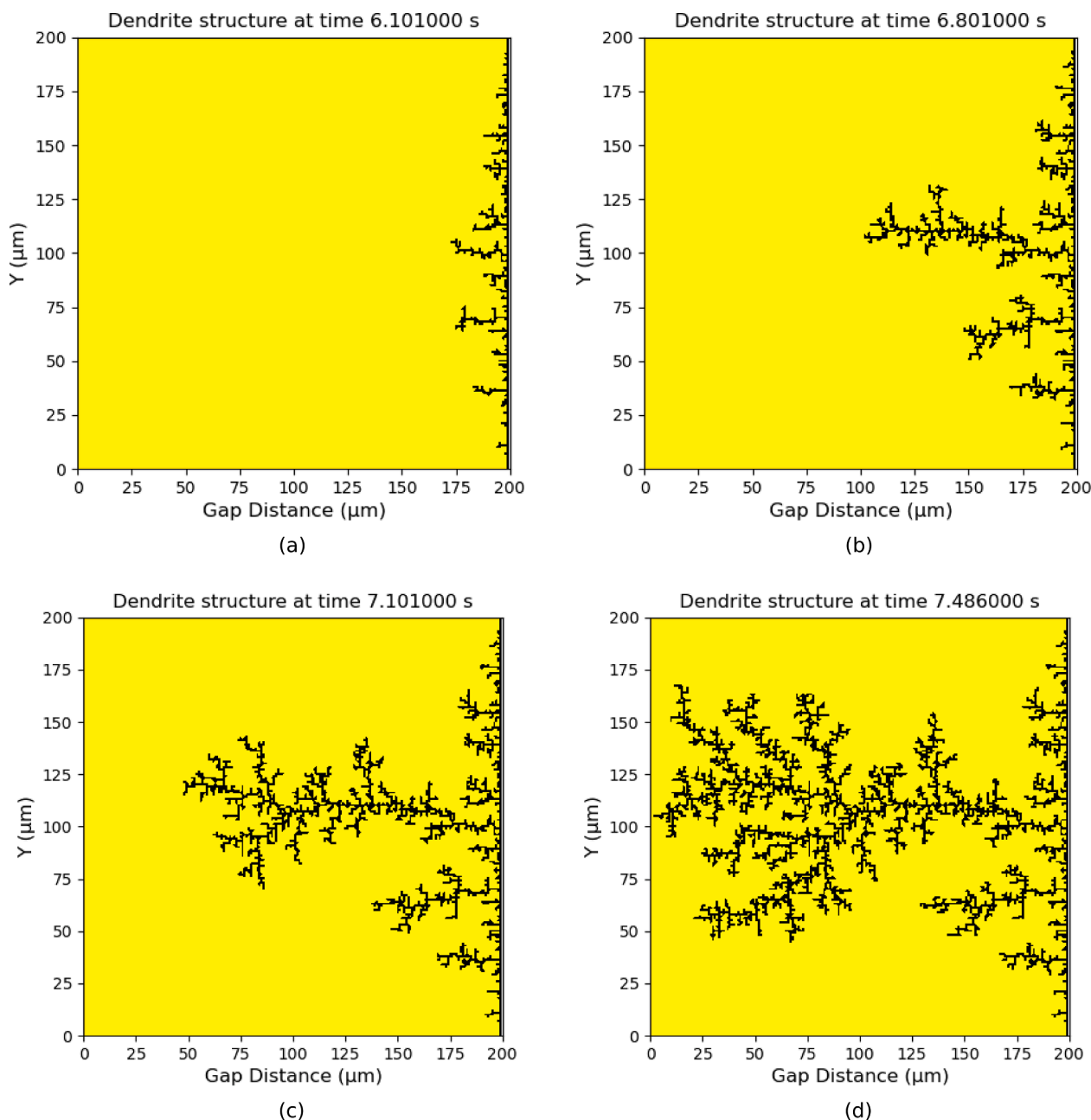

Fig. 5. Evolution of dendrites in the case of 200 μm gap distance (with 0 μm representing the anode and 200 μm the cathode) at: (a) 6.101 s, (b) 6.801 s, (c) 7.101 s, and (d) 7.486 s.
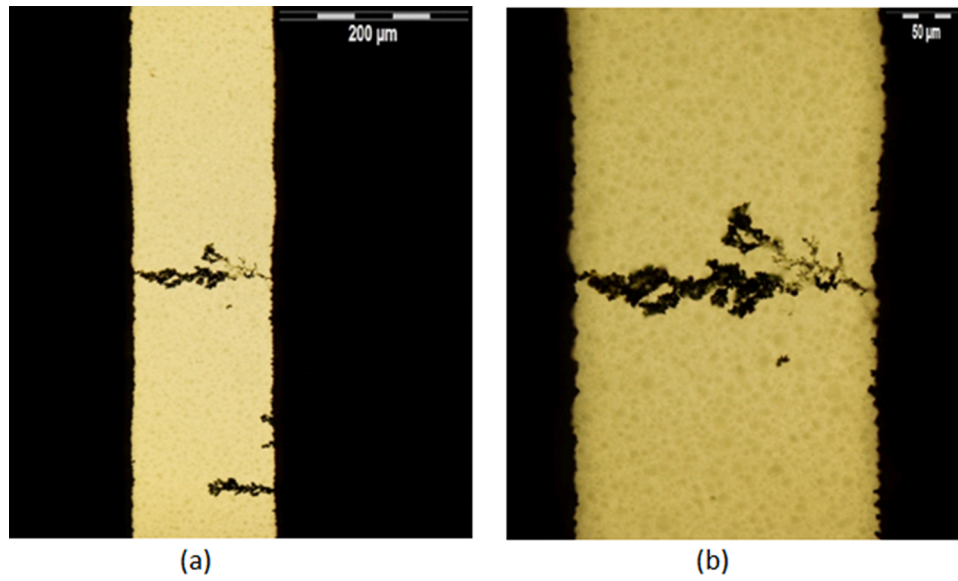
Fig. 6. Cu dendrites formed experimentally during the WD tests at 10 VDC using a DI water droplet: (a) completely formed Cu dendrite, and (b) a higher magnification of the dendrites highlighting the tree-like structure (anode is on the left and cathode is on the right).
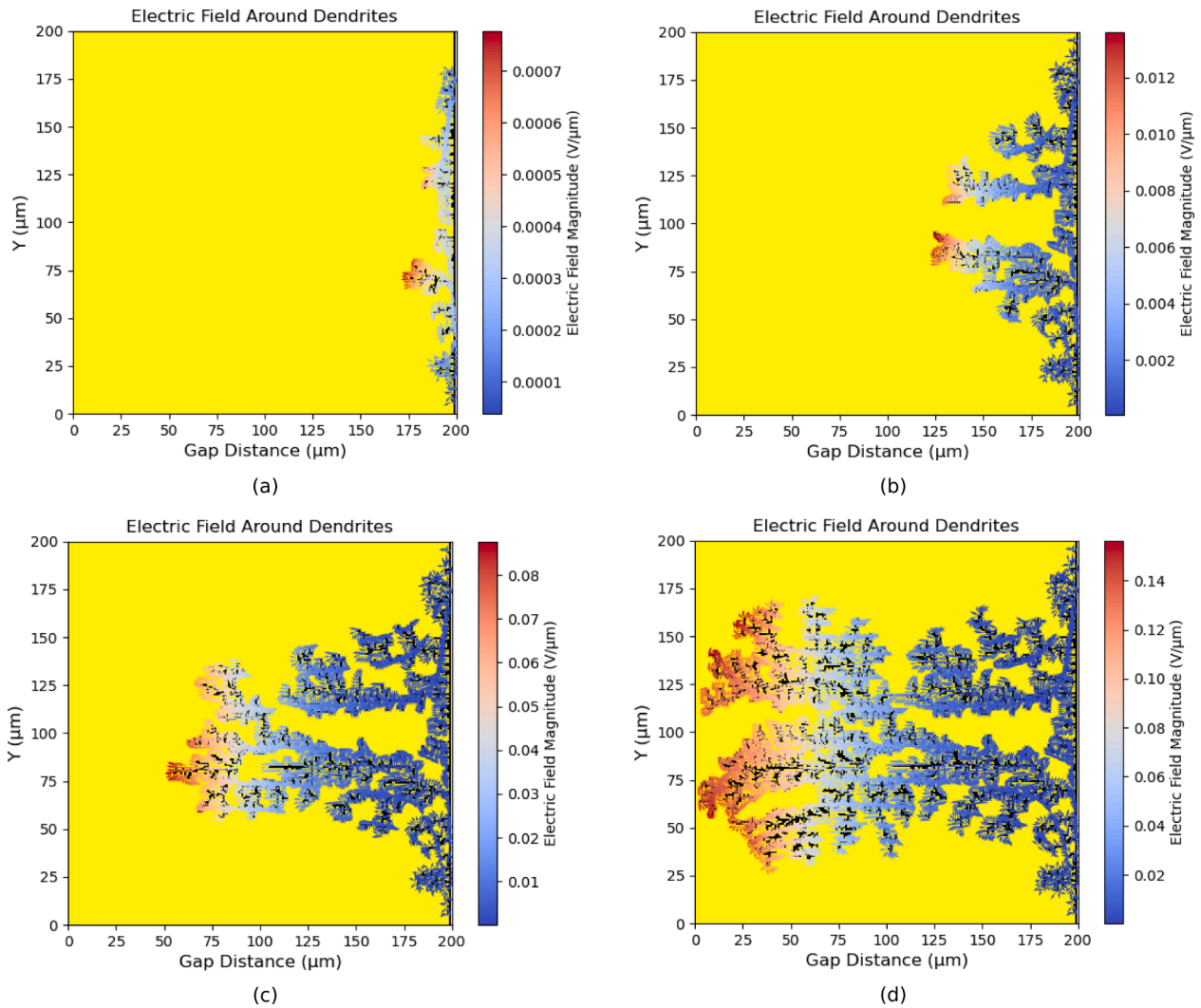

Fig. 7. Evolution of electric field magnitude around the dendrites in the case of 200 μm gap size (with 0 μm representing the anode and 200 μm the cathode) at: (a) 6.2 s, (b) 7 s, (c) 7.5 s, and (d) 8 s.

growth range [49]. However, this observation contrasts with the findings in [14], where concentrated dendrites were reported even at relatively higher voltages.

Fig. 7 visualizes the electric field distribution around the grown dendrites. The electric field magnitude at the tips of dendrites increases significantly over time and toward the anode, thereby raising the likelihood of dendrite growth. For example, the electric field intensifies by 15 times at 7 s (Fig. 7b) compared to 6.2 s, by 6 times at 7.5 s (Fig. 7c) relative to 7 s, and doubles again at 8 s (Fig. 7d). These changes highlight the critical role of electric field magnitude evolution in the dendrite growth process. Furthermore, it can be observed that the variations in the electric field across the surface can cause uneven deposition, encouraging branches to form and extend toward regions of higher field strength (Fig. 7d). This effect is due to the dendrites' tendency to grow along electric field lines, meaning that as the field intensifies, the dendrite structure adapts, forming complex branches. The analysis of the computed dendrite growth and electric field evolution suggests strong agreement with observed growth probabilities when the constants k_1 and k_2 are set to 0.5.

4. Conclusions

A 2D numerical ECM model was developed to study dendrite growth on pure copper electrodes in a contaminant-free electrolyte. The model combines deterministic methods for simulating anodic dissolution and ion transport, with stochastic methods for modeling dendrite growth. The numerical ECM model was validated by the TTF values and dendritic morphology from experimental data, and they showed good agreement. Numerical solutions of the Nernst–Planck equation revealed that during the incubation period, ion transport across the electrode gap follows an exponential pattern, regardless of the anodic dissolution mechanism. This exponential behavior stems from the diffusion and migration terms, which exhibit exponential profiles along the gap, with their relative contributions varying by position and time along the grid. Initially, diffusion dominates the ion transport, but over time, the migration term increases significantly, starting near the anode and progressively becoming more apparent toward the cathode. This trend over time suggests that neglecting migration term would be inappropriate when modeling ECM for longer incubation periods. The Monte Carlo simulation demonstrated both efficiency and flexibility in modeling dendrite growth resembling a tree-like structure, considering variations in concentration and the electric field along the grid. By randomizing the number of dendrite growth attempts per time step, the inherent randomness of the dendrite growth process was effectively incorporated into the model. Future work should focus on exploring the extension of the current model to account for the effects of contaminants on the copper ECM rate.

CRediT authorship contribution statement

Ali Dayoub: Writing – original draft, Software, Methodology, Data curation, Conceptualization. **Ali Gharaibeh:** Writing – original draft, Software, Methodology, Investigation, Data curation, Conceptualization. **Balázs Illés:** Writing – review & editing, Methodology, Formal analysis. **Bálint Medgyes:** Validation, Project administration, Conceptualization.

Declaration of competing interest

We wish to confirm that there are no known conflicts of interest associated with this publication, and there has been no significant financial support for this work that could have influenced its outcome.

Acknowledgment

Data availability

Data will be made available on request.

References

[1] X. Song, K. Wang, Z. Chen, K. Ren, P. Liu, Electrochemical migration behavior on FR-4 printed circuit board with different surface finishes, J. Electron. Mater. 52 (2023) 6121–6132, https://doi.org/10.1007/s11664-023-10557-w.
[2] E.L. Lee, Y.S. Goh, A.S.M.A. Haseeb, Y.H. Wong, M.F. Mohd Sabri, B.Y. Low, Review—Electrochemical migration in electronic materials: factors affecting the mechanism and recent strategies for inhibition, J. Electrochem. Soc. 170 (2023) 21505, https://doi.org/10.1149/1945-7111/acb61a.
[3] J.L. Barton, J.O. Bockris, The electrolytic growth of dendrites from ionic solutions, Proc. R. Soc. A 268 (1962) 485–505.
[4] A. Gharaibeh, B. Illes, A. Geczy, B. Medgyes, Numerical models of the electrochemical migration: a short review, in: 2020 IEEE 26th Int. Symp. Des. Technol. Electron. Packag., Pitesti, Romania, 2020, pp. 178–183, https://doi.org/10.1109/SIITME50350.2020.9292229.
[5] V. Verdingovas, M.S. Jellesen, R. Ambat, Effect of pulsed voltage on electrochemical migration of tin in electronics, J. Mater. Sci. Mater. Electron. 26 (2015) 7997–8007, https://doi.org/10.1007/s10854-015-3454-9.
[6] H. Conseil-Gudla, M.S. Jellesen, R. Ambat, Printed circuit board surface finish and effects of chloride contamination, electric field, and humidity on corrosion reliability, J. Electron. Mater. 46 (2017) 817–825, https://doi.org/10.1007/s11664-016-4974-7.
[7] D. Minzari, M.S. Jellesen, P. Møller, R. Ambat, On the electrochemical migration mechanism of tin in electronics, Corros. Sci. 53 (2011) 3366–3379, https://doi.org/10.1016/j.corsci.2011.06.015.
[8] D.Q. Yu, W. Jillek, E. Schmitt, Electrochemical migration of Sn-Pb and lead free solder alloys under distilled water, J. Mater. Sci. Mater. Electron. 17 (2006) 219–227, https://doi.org/10.1007/s10854-006-6764-0.
[9] G.T. Kohman, H.W. Hermance, G.H. Downes, Silver migration in electrical insulation, Bell Syst. Tech. J. 34 (1955) 1115–1147.
[10] B. Medgyes, B. Illés, G. Harsányi, Electrochemical migration behaviour of Cu, Sn, Ag and Sn63/Pb37, J. Mater. Sci. Mater. Electron. 23 (2012) 551–556, https://doi.org/10.1007/s10854-011-0435-5.
[11] Y. Chen, J. Wang, J. Wang, F. Tian, H. Chen, M. Li, Y. Chen, J. Wang, J. Wang, S. Li, F. Tian, H. Chen, G. Peng, Corrosion resistance and electrochemical migration behavior of InSnBiAgxZn low-melting-point alloy solders, J. Mater. Res. Technol. 32 (2024) 792–801, https://doi.org/10.1016/j.jmrt.2024.07.151.
[12] X. Zhong, S. Yu, L. Chen, J. Hu, Z. Zhang, Test methods for electrochemical migration: a review, J. Mater. Sci. Mater. Electron. 28 (2017) 2279–2289, https://doi.org/10.1007/s10854-016-5713-9.
[13] X. Zhong, L. Chen, B. Medgyes, Z. Zhang, S. Gao, L. Jakab, Electrochemical migration of Sn and Sn solder alloys: a review, RSC Adv. 7 (2017) 28186–28206, https://doi.org/10.1039/c7ra04368f.
[14] B. Medgyes, A. Gharaibeh, D. Rigler, G. Harsányi, On the electrochemical migration mechanism of gold in electronics—Less reliable than expected? Materials (Basel) 14 (2021) 5237, https://doi.org/10.3390/ma14185237.
[15] M. Klimtova, P. Vesely, I. Kralova, Y.H. Wong, M.F. Mohd Sabri, K. Dusek, Electrochemical migration resistance of gold surface finishes, in: 2024 47th Int. Spring Semin. Electron. Technol., Prague, Czech Republic, 2024, pp. 1–5, https://doi.org/10.1109/ISSE61612.2024.10604108.
[16] S. Yang, A. Christou, Failure model for silver electrochemical migration, IEEE Trans. Device Mater. Reliab. 7 (2007) 188–196, https://doi.org/10.1109/TDMR.2007.891531.
[17] Y. Zhou, Y. Li, Y. Chen, M. Zhu, Life model of the electrochemical migration failure of printed circuit boards under NaCl solution, IEEE Trans. Device Mater. Reliab. 19 (2019) 622–629, https://doi.org/10.1109/TDMR.2019.2938010.
[18] Y. Zhou, Y. Chen, Q. Xie, Y. Li, Modeling research of electrochemical migration failure on printed circuit board, in: Proc. - 2018 Progn. Syst. Heal. Manag. Conf. PHM-Chongqing 2018, IEEE, 2019, pp. 209–214, https://doi.org/10.1109/PHM-Chongqing.2018.00042.
[19] Y. Zhou, L. Yang, Y. Li, W. Lu, Exploring the data-driven modeling methods for electrochemical migration failure of printed circuit board, in: Proc. - 2019 Progn. Syst. Heal. Manag. Conf. PHM-Paris 2019, IEEE, 2019, pp. 100–105, https://doi.org/10.1109/PHM-Paris.2019.00025.
[20] Y. Zhou, Y. Zhao, L. Yang, Y. Li, W. Lu, Data-driven life modeling of electrochemical migration on printed circuit boards under soluble salt contamination, IEEE Access. 8 (2020) 182580–182590, https://doi.org/10.1109/ACCESS.2020.3029200.
[21] J.N. Chazalviel, Electrochemical aspects of the generation of ramified metallic electrodeposits, Phys. Rev. A 42 (1990) 7355–7367, https://doi.org/10.1103/PhysRevA.42.7355.
[22] J.C. Bradley, S. Dengra, G.A. Gonzalez, G. Marshall, F.V. Molina, Ion transport and deposit growth in spatially coupled bipolar electrochemistry, J. Electroanal. Chem. 478 (1999) 128–139, https://doi.org/10.1016/S0022-0728(99)00424-6.

[23] V. Fleury, J.N. Chazalviel, M. Rosso, Theory and experimental evidence of electroconvection around electrochemical deposits, Phys. Rev. Lett. 68 (1992) 2492–2495, https://doi.org/10.1103/PhysRevLett.68.2492.

[24] V. Fleury, J.-N. Chazalviel, M. Rosso, Coupling of drift, diffusion, and electroconvection, in the vicinity of growing electrodeposits, Phys. Rev. E 48 (1993) 1279–1295.

[25] V. Fleury, J. Kaufman, B. Hibbert, Evolution of the space-charge layer during electrochemical deposition with convection, Phys. Rev. E 48 (1993) 3831–3840.

[26] V. Fleury, J.H. Kaufman, D.B. Hibbert, Mechanism of a morphology transition in ramified electrochemical growth, Nature 367 (1994) 435–438, https://doi.org/10.1038/367435a0.

[27] X. He, M.H. Azarian, M.G. Pecht, Analysis of the kinetics of electrochemical migration on printed circuit boards using Nernst–Planck transport equation, Electrochim. Acta 142 (2014) 1–10, https://doi.org/10.1016/j.electacta.2014.06.041.

[28] X. He, M.H. Azarian, M.G. Pecht, Evaluation of electrochemical migration on printed circuit boards with lead-free and tin-lead solder, J. Electron. Mater. 40 (2011) 1921–1936, https://doi.org/10.1007/s11664-011-1672-3.

[29] B. Illés, B. Medgyes, K. Dušek, D. Bušek, A. Skwarek, A. Géczy, Numerical simulation of electrochemical migration of Cu based on the Nernst–Plank equation, Int. J. Heat Mass Transf. 184 (2022) 122268, https://doi.org/10.1016/j.ijheatmasstransfer.2021.122268.

[30] C. Cao, M. Yang, C. Liang, D. Zhang, X. Chen, X. Zhao, C.C. Lee, Y. Huo, A phase-field model of electrochemical migration for silver-based conductive adhesives, Electrochim. Acta 471 (2023) 143388, https://doi.org/10.1016/j.electacta.2023.143388.

[31] H. Ma, A. Kunwar, J. Chen, L. Qu, Y. Wang, X. Song, P. Råback, H. Ma, N. Zhao, Study of electrochemical migration based transport kinetics of metal ions in Sn-9Zn alloy, Microelectron. Reliab. 83 (2018) 198–205, https://doi.org/10.1016/j.microrel.2018.02.013.

[32] P. Xue, A.S. Bahman, F. Iannuzzo, H.C. Gudla, A.R. Lakkaraju, R. Ambat, Prediction of the electrochemical migration induced failure on power PCBs under humidity condition—A case study, Microelectron. Reliab. 139 (2022) 114796, https://doi.org/10.1016/j.microrel.2022.114796.

[33] Z.Ható, B. Horváth, S. Guba, Z. Tóth, E. Kocsis, D. Boda, I. Szalai, Electrochemical migration and dendrite growth between two electrodes: experiments and Brownian dynamics simulations, Int. J. Heat Mass Transf. 234 (2024) 126108, https://doi.org/10.1016/j.ijheatmasstransfer.2024.126108.

[34] S. Oh, D. Kim, W. Hong, K. Kim, C. Oh, Copper electrochemical migration growth in an air HAST, Microelectron. Reliab. (2019) 100–101, https://doi.org/10.1016/j.microrel.2019.06.086.

[35] Y. Zhou, P. Yang, C. Yuan, Y. Huo, Electrochemical migration failure of the copper trace on printed circuit board driven by immersion silver finish, Chem. Eng. Trans. 33 (2013) 559–564, https://doi.org/10.3303/CET1333094.

[36] X. Chen, L. Chen, Y. Wang, D. Luo, J. Chen, B. Zhu, Contaminant and alcohol induced electrochemical migration of Au bond in ICs during low temperature operation test, in: 2018 IEEE Int. Symp. Phys. Fail. Anal. Integr. Circuits, 2018, pp. 1–4, https://doi.org/10.1109/IPFA.2018.8452581.

[37] W.M. Haynes, CRC Handbook of Chemistry and Physics, 93rd ed., CRC Press, New York, 2012.

[38] A. Aryanfar, D. Brooks, B.V. Merinov, W.A. Goddard, A.J. Colussi, M.R. Hoffmann, Dynamics of lithium dendrite growth and inhibition: pulse charging experiments and Monte Carlo calculations, J. Phys. Chem. Lett. 5 (2014) 1721–1726, https://doi.org/10.1021/jz500207a.

[39] J. Szép, J. Cserti, J. Kertész, Monte Carlo approach to dendritic growth, J. Phys. A. Math. Gen. 18 (1985) L413–L418, https://doi.org/10.1088/0305-4470/18/8/002.

[40] F. Li, V. Verdingovas, K. Dirscherl, G. Harsányi, B. Medgyes, R. Ambat, Influence of Ni, Bi, and Sb additives on the microstructure and the corrosion behavior of Sn–Ag–Cu solder alloys, J. Mater. Sci. Mater. Electron. 31 (2020) 15308–15321, https://doi.org/10.1007/s10854-020-04095-y.

[41] D. Ulbrich, J. Selech, J. Kowalczyk, J. Jóźwiak, K. Durczak, L. Gil, D. Pieniak, M. Paczkowska, K. Przystupa, Reliability analysis for unrepairable automotive components, Materials (Basel) 14 (2021) 7014, https://doi.org/10.3390/ma14227014.

[42] A. Gharaibeh, D. Rigler, B. Medgyes, Effect of TiO$_2$ nanoparticles addition on the electrochemical migration of low-silver lead-free SAC alloys, in: 2023 46th Int. Spring Semin. Electron. Technol., Timişoara, Romania, 2023, pp. 1–5, https://doi.org/10.1109/ISSE57496.2023.10168444.

[43] B.I. Noh, J.W. Yoon, W.S. Hong, S.B. Jung, Evaluation of electrochemical migration on flexible printed circuit boards with different surface finishes, J. Electron. Mater. 38 (2009) 902–907, https://doi.org/10.1007/s11664-009-0737-z.

[44] K. Qi, H. Huang, Electrochemical migration behavior of copper under a thin distilled water layer, Corros. Commun. 11 (2023) 52–57, https://doi.org/10.1016/j.corcom.2022.09.004.

[45] B. Medgyes, X. Zhong, G. Harsányi, The effect of chloride ion concentration on electrochemical migration of copper, J. Mater. Sci. Mater. Electron. 26 (2015) 2010–2015, https://doi.org/10.1007/s10854-014-2640-5.

[46] L. Hua, C. Yang, Corrosion behavior, whisker growth, and electrochemical migration of Sn-3.0Ag-0.5Cu solder doping with In and Zn in NaCl solution, Microelectron. Reliab. 51 (2011) 2274–2283, https://doi.org/10.1016/j.microrel.2011.06.023.

[47] X. Qi, H. Ma, C. Wang, S. Shang, X. Li, Y. Wang, H. Ma, Electrochemical migration behavior of Sn-based lead-free solder, J. Mater. Sci. Mater. Electron. 30 (2019) 14695–14702, https://doi.org/10.1007/s10854-019-01841-9.

[48] Y.K. Kwok, C.C.K. Wu, Numerical simulation of electrochemical diffusion-migration model with reaction at electrodes, Comput. Methods Appl. Mech. Eng. 132 (1996) 305–317, https://doi.org/10.1016/0045-7825(96)01033-X.

[49] Y. Choi, K.-Y. Chan, Exact solutions of transport in a binary electrolyte, J. Electroanal. Chem. 334 (1992) 13–23.